Cross-Beam Energy Transfer Saturation: Ion Heating and Pump Depletion

A. M. Hansen[1,2], K. L. Nguyen[1,2,3], D. Turnbull[1], B. J. Albright[3], R. K. Follett[1], R. Huff[1], J. Katz[1], D. Mastrosimone[1], A. L. Milder[1,2], L. Yin[3], J. P. Palastro[1], D. H. Froula[1]

[1]Laboratory for Laser Energetics, University of Rochester, 250 East River Road, Rochester, New York 14623, USA
[2]Department of Physics and Astronomy, University of Rochester, Rochester, New York 14623, USA
[3]Los Alamos National Laboratory, Los Alamos, New Mexico 87545, USA

E-mail: ahan@lle.rochester.edu

DATE

Abstract. Cross-beam energy transfer (CBET) was measured in two regimes where the energy transfer saturation mechanism was determined by the plasma and laser beam conditions. Linear kinetic CBET theory agreed well with the measured energy transfer in all experiment configurations and at all probe beam intensities when accounting for pump depletion and the plasma conditions measured using Thomson-scattering. Simultaneous CBET and Thomson-scattering measurements enabled uncertainties in the plasma conditions to be isolated from CBET theory, which allowed the saturation mechanisms to be identified. In the perpendicular-beam configuration the saturation mode was through ion heating, which resulted from ion trapping in the driven waves and subsequent ion-ion collisional heating. In the co-propagating beam configuration there was minimal ion heating and the saturation mode was through pump depletion.

1. Introduction

In all forms of laser-driven inertial confinement fusion (ICF), the drive laser beams must propagate through regions of underdense plasma where they are susceptible to laser-plasma instabilities (LPI). Cross-beam energy transfer (CBET) occurs when the electromagnetic beat-wave between two laser beams ponderomotively drives an ion-acoustic wave (IAW) that scatters laser light from one beam to the other [1]. This instability decreases laser beam absorption in direct-drive ICF [2] and can impact drive uniformity in indirect-drive ICF experiments [3, 4]. The radiation hydrodynamic simulations used to predict the performance of ICF experiments typically implement linear CBET models. These simplified models require ad hoc multipliers on the linear CBET theory to match experimental observables [5, 6]. As a result, these multipliers may mask important physical processes and hinder the predictive capabilities of the models in ICF design spaces outside of those experimentally tested. An understanding of energy transfer saturation mechanisms and the feedback that LPI has on the plasma conditions that control the instabilities is critical for the development of predictive CBET models.

CBET is resonant when the frequency of the electromagnetic beat wave created by the crossing beams is equal to the frequency of the ion-acoustic wave, which occurs when $\omega_b = |\mathbf{k}_b|c_s$ where c_s is the sound speed, $\mathbf{k}_b = \mathbf{k}_0 - \mathbf{k}_1$ is the beat wave wavevector, and $\omega_b = \omega_0 - \omega_1$ is the beat wave frequency; subscripts 0 and 1 refer to the pump and probe laser beams respectively. When the interaction is at resonance, the normalized driven IAW amplitude can grow to large amplitudes and scatter significant amounts of energy between the crossed laser beams. The growth of the driven waves and the amount of energy transferred in these interactions is limited at high-probe beam intensities by CBET saturation.

CBET saturation has been observed in past experiments, but limitations in the measurement of plasma conditions prevented a full characterization of the specific saturation mechanism [7, 8, 9]. Simulations using particle-in-cell and Vlasov codes have predicted that at large ion-wave amplitudes ($\delta n/n \gtrsim 1\%$), nonlinear processes will impact the wave behavior, resulting in deviations from the kinetic linear theory on short timescales [10, 11, 12]. These studies suggest that kinetic wave-particle effects can lead to saturation thresholds that are significantly lower than the thresholds predicted by fluid theory [13]. On hydrodynamic timescales, however, CBET has been predicted to result in ion-heating, which detunes the CBET instability [5, 14].

The frequency matching condition for CBET conserves energy in the photon scattering process, where the energy differential between the incident and scattered photons is absorbed by a plasma phonon with energy $\hbar\omega_b = \hbar\omega_0 - \hbar\omega_1$ [15]. On sufficiently long timescales, the energy absorbed by the plasma phonons will be thermalized, leading to an increase in the plasma temperature. In the regime where ion Landau damping dominates the ion-acoustic wave damping, the absorbed phonon energy will result in an increase in ion temperatures [5, 14, 16, 17]. The significance of this ion heating can be characterized by the rate of the ion heating due to CBET normalized to the total ion thermal energy within the overlapped beam volume,

$$\gamma = \frac{2\eta I_1^i (e^G - 1)}{3Ln_iT_i}, \tag{1}$$

where $G = \ln(I_1^f/I_1^i)$ is the CBET gain, I_1^i and I_1^f are the initial and final probe beam intensities, respectively, L is the CBET interaction length, $\eta = \omega_b/\omega_1$ is the CBET scattering energy efficiency, n_i is the ion number density, and T_i is the ion temperature. In the case of multiple pump beams, the total gain in the probe beam is the linear superposition of the gain from each pump-probe beam combination, and therefore significant ion heating can occur even for low-gain single-beam CBET interactions when many beams are overlapped.

Here, we used Thomson scattering to measure the plasma conditions during CBET experiments using the LPI Platform on the OMEGA laser [18], which allowed

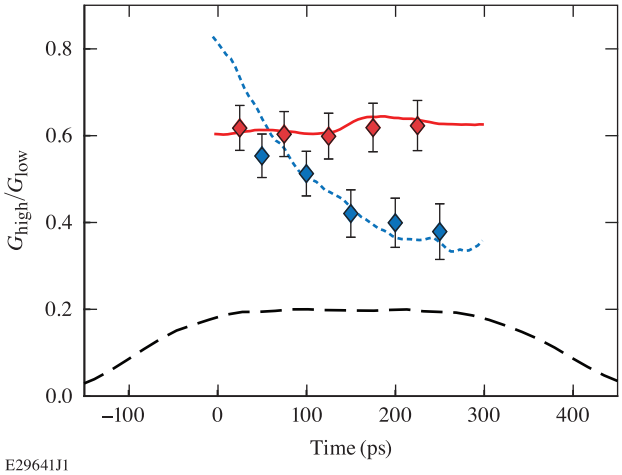

Figure 1. The normalized measured time-resolved CBET gains for the high- (blue dashed curve, $\gamma = 0.024$ ps^{-1}) and low- (red solid curve, $\gamma = 0.008$ ps^{-1}) ion-heating rate configurations. The high-intensity ($I \sim 2 \times 10^{14}$ W/cm^2) gains (G_{high}) were normalized to the low-intensity ($I \leq 0.1 \times 10^{14}$ W/cm^2) gains (G_{low}) measured in the identical corresponding configurations. The diamonds represent the gain predicted using linear kinetic CBET theory when accounting for the Thomson-scattering measured plasma conditions and pump depletion effects. The long-dashed black curve shows the shape of the pump-beam pulse (normalized arbitrarily).

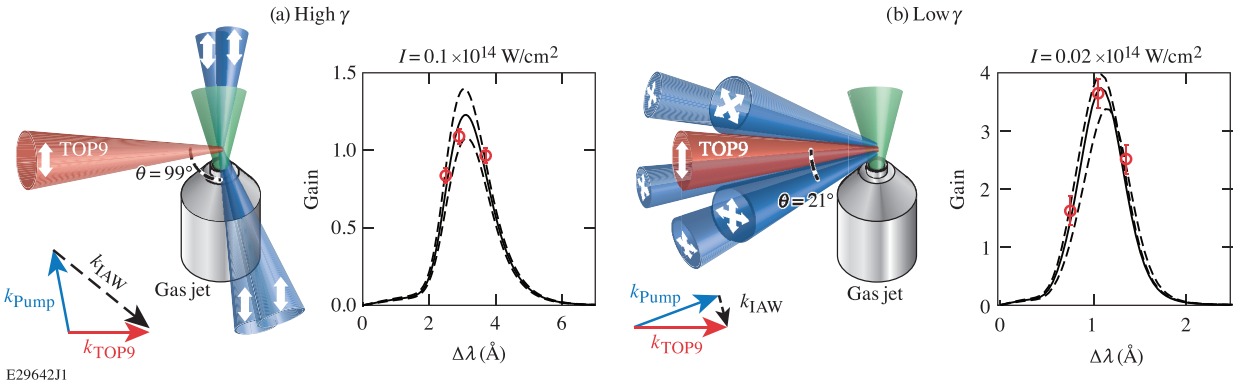

Figure 2. The beam setups and low-probe beam intensity wavelength scans for the (a) high- and (b) low-ion-heating rate CBET configurations. The measured (red circles) and calculated (black solid curve) CBET gains at low-probe intensities were used to determine the wavelength shift ($\Delta\lambda_{peak}$) where the peak gain occurred. The dashed-black curves show the uncertainties in the gain calculations propagated from the uncertainties in the measured plasma conditions. The polarization of the pump beams were nearly s-polarized linear (white arrow) and polarization smoothed (white-crossed arrows) for the high- and low-ion-heating rate configurations, respectively. Table 1 further details the differences between the two configurations.

the saturation of CBET to be clearly identified and the mechanisms determined (Fig. 1). By normalizing the measured gains obtained from experiments that used a high-intensity probe beam to the gains measured with low-probe beam intensities (G_{high}/G_{low}), saturation could be clearly identified — a reduction below unity is a direct indication of CBET saturation ($G_{high}/G_{low} < 1$). In the high-ion-heating rate configuration, the experiments demonstrate saturation, both through a reduction in the normalized gain at early times and a significant reduction as a function of time (Fig. 1). This is contrasted with the low-ion-heating rate configuration where the high-intensity gain was reduced, but it remained nearly constant throughout the measurements. Calculated linear kinetic CBET [5] gains, when including the nearly constant measured plasma conditions and saturation through pump depletion, are in excellent agreement with the CBET measurements at all times. In the high-ion-heating rate configuration, where pump depletion did not play a role in the saturation process, the ion temperature was measured to increase by a factor of seven over the 300 ps when CBET was active. When using these measured plasma conditions to calculate the linear kinetic CBET gains, excellent agreement was found at all times, demonstrating that the saturation mechanism in the high-ion-heating rate configuration was a result of ion heating by CBET.

In a previous publication, we used Thomson-scattering to demonstrate the saturation of energy transfer through ion heating [17]. In this work, we have demonstrated how the pump beam settings determine the saturation mechanism and control the level of feedback from CBET on the plasma conditions. This feedback on plasma conditions was measured as a probe-intensity dependent heating of the ions in the high-ion-heating configuration. For the low-ion-heating configuration, the feedback on plasma conditions was minimal and the energy transfer was limited by the depletion of the pump beams' intensity. Particle-in-cell simulations showed that on CBET timescales, nonlinear trapping and collisional effects lead to the ion heating on hydrodynamic timescales, which limits energy transfer and reduces the interactions to the regime where linear kinetic CBET models reproduce the energy transfer. These experiments demonstrate the robustness of linear kinetic CBET models used in most ICF hydrodynamic simulations when plasma conditions and pump depletion effects are accurately determined. They also show the need to accurately model the feedback of LPI on the plasma conditions, effects that are typically neglected in integrated hydrodynamic simulations.

2. Experimental Setup

2.1. Beam and Target Configuration

The LPI platform on OMEGA used a gas-jet system with a Mach 2.6 supersonic nozzle and a 2-mm exit diameter to produce a plume of neutral gas, which was subsequently heated by nine 351-nm beams [18, 19]. The heating beams were 500-ps long flattop pulses that used phase plates to produce large round spots spots [850 μm full-width half-maximum (FWHM)] with a total overlapped intensity of $\sim 6 \times 10^{14}$ W/cm^2. The target gas was a mixture of 45% nitrogen and 55% hydrogen. The plasma conditions produced in this setup after the heating phase are summarized in Table 1.

After a $\sim$ 250 ps delay following the end of the heating beam pulse, the Tunable OMEGA Port 9 (TOP9) laser [20] was crossed with several UV pump beams in the gas-jet plasma. The TOP9 laser was an

upgrade to the OMEGA EP system that provided a wavelength tunable beam between 350.2 to 353.4 nm to be delivered to the OMEGA target chamber [20]. The TOP9 beam used a 1.5-ns and 2.4-ns square pulse shape for the high- and low-ion-heating configurations, respectively. The TOP9 beam was linear polarized and aligned nearly parallel to the pump beams' polarization in the high-ion-heating configuration as illustrated in Fig. 1(a). The TOP9 beam used a phase plate that set the spot size to be round with a 1/e diameter of 160 μm. The intensity in the TOP9 beam was varied between 0.02×10^{14} W/cm^2 and 4.1×10^{14} W/cm^2 to study CBET in both the unsaturated and saturated CBET regimes.

The pump beam array was used in either the high- or low-ion-heating configuration as illustrated in Fig. 2. The OMEGA laser geometry and available polarization schemes determined the number of pump beams and the beam polarization used in each configuration. The pump beams were chosen to interact identically with the TOP9 probe beam within each configuration.

The beam crossing angle and pump beam polarization were varied between the two configurations to produce CBET saturation at high TOP9 beam intensities either through ion-heating or through pump depletion. The high-ion-heating configuration used four UV pump beams [Fig. 2(a)] where each beam formed a $\theta = 99^\circ$ angle with respect to the the TOP9 probe beam's propagation vector. The pump beams used linear polarizations that were nearly aligned with the TOP9 probe beam's polarization. The low-ion-heating configuration used five UV pump beams [Fig. 2(b)] where each beam formed a $\theta = 21^\circ$ angle with the TOP9 probe beam. In this configuration the pump beams used polarization smoothing, which produced spots where the beam intensity was split evenly between two perpendicular polarizations [21]. In both configurations, the pump beams used the 500-ps long-pulse shape shown in Fig. 1, with phase plates that produced elliptical spots with 1/e minor radii of 106 μm and 1/e major radii of 145 μm. In the low-ion-heating configuration, each of the five pump beams had an intensity of $\sim 8.3 \times 10^{14}$ W/cm^2. Due to geometry constraints, in the high-ion-heating configuration the four pump beams were separated into two pairs: the high- and a low-angle beams. The high-angle beams each had intensities of $\sim 8.3 \times 10^{14}$ W/cm^2 and their polarization vectors formed 23° and -23° angles with the TOP9 beam polarization. The low-angle beams each had intensities of $\sim 7.5 \times 10^{14}$ W/cm^2 and their polarization vectors formed 13° and -13° angles with the TOP9 beam polarization.

The length of the CBET interaction along the TOP9 probe beam [$L = d/\sin(\theta)$] was set by the beam crossing angle θ and the average width of the pump beam presented to the probe beam d [22]. This average pump beam width was found by integrating over the common intersecting beam volume at perpendicular incidence and dividing by the probe beam area. For the high-ion-heating configuration, the elliptical pump beam spots were oriented such that the major axis was perpendicular to the probe beam's axis. In this configuration the 99^o crossing angle set the average probe beam CBET interaction length to $L \simeq 210$ μm. For the low-ion-heating configuration, the elliptical pump beam spots were randomly oriented and the 21^o crossing angle set the average probe beam CBET interaction length to $L \simeq 640$ μm.

Table 1. Initial plasma and beam conditions where $n_{cr,3\omega} = \omega_{pe}^2/\omega_{3\omega}^2$ is the critical density for 3ω light, ω_{pe} is the electron plasma frequency, and $\omega_{3\omega}$ is the frequency of the heater beams. T_e and T_i are the electron and ion temperatures measured with Thomson scattering prior to CBET. $v_{ph}/v_{th,H}$ is the ratio of the phase velocity of the weakest ion-acoustic mode normalized to the thermal velocity for the hydrogen ions. G_0 is the linear kinetic CBET gain at the peak of the resonance found at the wavelength detuning $\Delta\lambda_{peak}$ at low probe beam intensities.

Parameter	High γ	Low γ
$n_e/n_{cr,3\omega}$	0.007	0.010
T_e (eV)	600	800
T_i (eV)	150	150
$v_{ph}/v_{th,H}$	1	2
$\Delta\lambda_{peak}$ (Å)	2.9	1.1
Peak G_0	1.2	3.7
η	0.0008	0.0003
L (μm)	~ 210	~ 640
θ	99°	21°

2.2. Transmitted Beam Diagnostic

The TOP9 laser was characterized before and after the CBET interaction using the P9 transmitted beam diagnostic (P9TBD) [23]. The P9TBD used a spectralon diffuser with a diameter equal to twice the TOP9 nearfield diameter, which was located opposite the TOP9 beam port. A streaked spectrometer system measured the power in the TOP9 beam at two locations: after the CBET interaction from the light scattered from the diffuser and before the CBET interaction using a TOP9 beam pickoff. The gain in the CBET interaction was characterized by comparing the power in the TOP9 pulse shapes measured before and after the CBET interaction.

2.3. Thomson Scattering

The plasma conditions produced in the gas-jet were measured using the streaked Thomson-Scattering

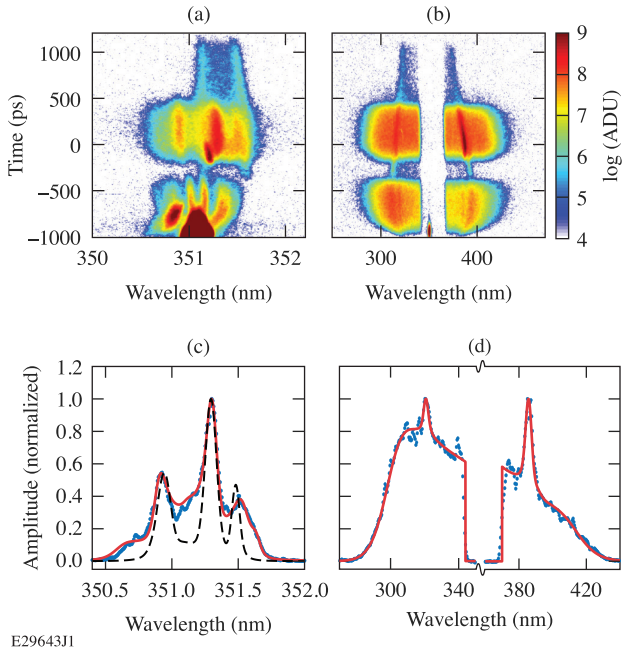

Figure 3. The measured time-resolved (a) IAW and (b) EPW spectrum for a high-ion-heating CBET configuration experiment where the TOP9 beam intensity was high ($I_1 = 4.1 \times 10^{14}$ W/cm^2). Spectrum of the (c) IAW and (d) EPW features at t=300 ps. The high-ion temperature ($T_{i,N} = 1100$ eV, $T_{i,H} = 640$ eV) calculated spectrum (solid red curve) is in good agreement with the data (blue points). The low-ion temperature ($T_{i,N} = 150$ eV, $T_{i,H} = 150$ eV) spectrum (dashed black curve) that used the ion temperature prior to ion heating by CBET is in poor agreement with the measured IAW spectrum.

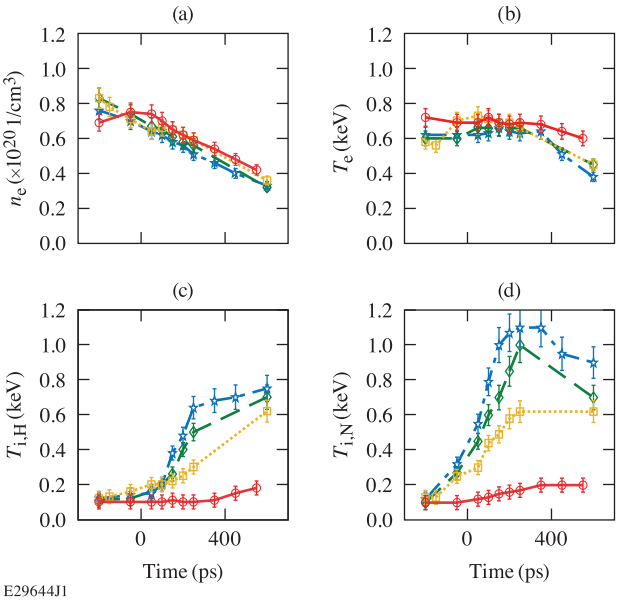

Figure 4. The time-resolved (a) electron density, (b) electron temperature, (c) hydrogen ion temperature, and (d) nitrogen ion temperature measured in the high-ion-heating configuration for a range of TOP9 beam intensities [0.1×10^{14} W/cm^2 (red circle points), 0.9×10^{14} W/cm^2 (yellow box points), 2.0×10^{14} W/cm^2 (green diamond points), 4.1×10^{14} W/cm^2 (blue star points)].

System (TSS) [24]. The f/10 TSS telescope collected the light scattered 60° from the TOP9 beam's propagation direction from a $\sim 200 \times 60 \times 60$ μm^3 region in space defined by the beam width and the diagnostic aperture stops. The TSS diagnostic consists of two coupled streak camera-spectrometer pairs, which resolved the spectral features associated with the ion acoustic wave (IAW) and electron plasma wave (EPW). The temporal resolutions were $\sim$ 100 ps, and the spectral resolutions were 0.02 nm and 0.5 nm for the IAW and EPW systems, respectively. The EPW system used a notch filter to reject the light near the laser wavelength at 351 nm.

Figure 3 shows the Thomson-scattered spectra from a high TOP9 beam intensity experiment in the high-ion-heating CBET configuration. Early in time ($t = -900$ ps to $t = -400$ ps) the measured signal was dominated by the light scattered from the nine heater beams as they formed a plasma in the gas-jet plume. Later in time ($t = -100$ ps to $t = 400$ ps) the measured signal was dominated by the light scattered from the CBET pump beams. After the pump beams were turned off ($t > 500$ ps), the light scattered from the TOP9 beam was apparent. The range of probed k-vectors associated with the set of CBET pump beams produces a scattered signal with a set of features demonstrating different degrees of collective behavior in the EPW spectrum and varied peak separations in the IAW spectrum.

Figures 3(c-d) show the Thomson-scattering spectra collected after the ions were heated by the CBET interaction. The sensitivity to ion temperature is evident in the shape of the peaks in the IAW feature; when comparing the calculated spectrum for the ion temperatures prior to the CBET interaction (t $\sim$ 0 ns) a significant difference is observed, demonstrating the sensitivity of the IAW spectrum to the changes in the ion temperature. The time-resolved Thomson-scattering spectra were calculated numerically using the standard multi-species collisionless spectral density function, which accounted for non-Maxwellian electron distribution functions [25, 26].

2.4. Plasma Conditions

Figure 4 shows the time-resolved plasma conditions measured in the high-ion-heating configuration for a range of initial TOP9 beam intensities. The electron densities and temperatures were consistent and show no significant dependence on the TOP9 beam intensity. Here, the electron plasma conditions were primarily determined by the pump beams ($I_{0,Total} \simeq 3.2 \times 10^{15}$ W/cm^2), which were significantly more intense than the TOP9 probe beam ($I_1 \leq 0.4 \times 10^{15}$ W/cm^2).

Table 1 summarizes the nominal initial plasma

conditions measured in the high- and low-ion-heating configurations. The gas-fill pressure was lower for the high-ion-heating configuration, which produced a plasma with a lower electron density and temperature. The initial (t$\sim$ 0 ns) ion temperatures were comparable between the two configurations and were significantly lower than the electron temperatures ($T_e/T_i \sim 5$), which is typical of laser-heated underdense gas-jet plasmas; the laser energy is absorbed by the electrons through inverse bremsstrahlung heating and the electrons collisionally heat the ions. The hydrodynamic expansion of the gas-jet plasma over the duration of the CBET interaction caused the electron density to drop by $\sim 20\%$ [Fig. 4(a)] and the electron temperature to drop by $\sim 10\%$ [Fig. 4(b)].

The measured temperatures in the high-ion-heating configuration indicate significant anomalous time-dependent ion heating that was correlated with the TOP9 beam intensity [Fig. 4(c-d)]. At the lowest TOP9 intensity (0.1×10^{14} W/cm^2, $\gamma = 0.001$ ps^{-1}), minimal heating of the ions was observed. At the highest TOP9 intensity (4.1×10^{14} W/cm^2, $\gamma = 0.044$ ps^{-1}), both the ion species rapidly heat, and the nitrogen ion temperatures exceeded the electron temperature by a factor of ~ 2 by the end of the CBET interaction ($t = 300$ ps). For each of the high-intensity ($I_1 \gtrsim 1 \times 10^{14}$ W/cm^2) TOP9 shots, the most rapid heating occurred over the time-period where CBET was most active ($0 - 300$ ps) and in every case the nitrogen ions heated more quickly than the hydrogen ions. In the low-ion-heating configuration, the ion temperature increased modestly, consistent with the expected heating from electron-ion thermalization.

3. CBET Results

3.1. CBET Measurements

Figure 5 shows CBET saturation was observed in both configurations as a decrease in the measured gain $G = \ln(I_1^f/I_1^i)$ relative to the gain measured from the lowest intensity shot, which was assumed to have no saturation effects. In the high-ion-heating configuration [Fig. 5(a)], the CBET saturation was strongly intensity- and time-dependent. The measured gains rapidly dropped from $t = 0$ to $t \sim 150$ ps before plateauing until $t \sim 300$ ps. In the low-ion-heating configuration [Fig. 5(b)], the CBET saturation was intensity dependent, but the gains for each shot were nearly constant in time from $t = 0$ to $t = 300$ ps.

Figure 6(a) shows the normalized gains measured near the end of the interaction ($t = 300$ ps) in both CBET configurations. Here the gains were normalized to the gain measured in the lowest TOP9 intensity shots. In both the high- and low-ion-heating configurations, the energy transfer saturates as the

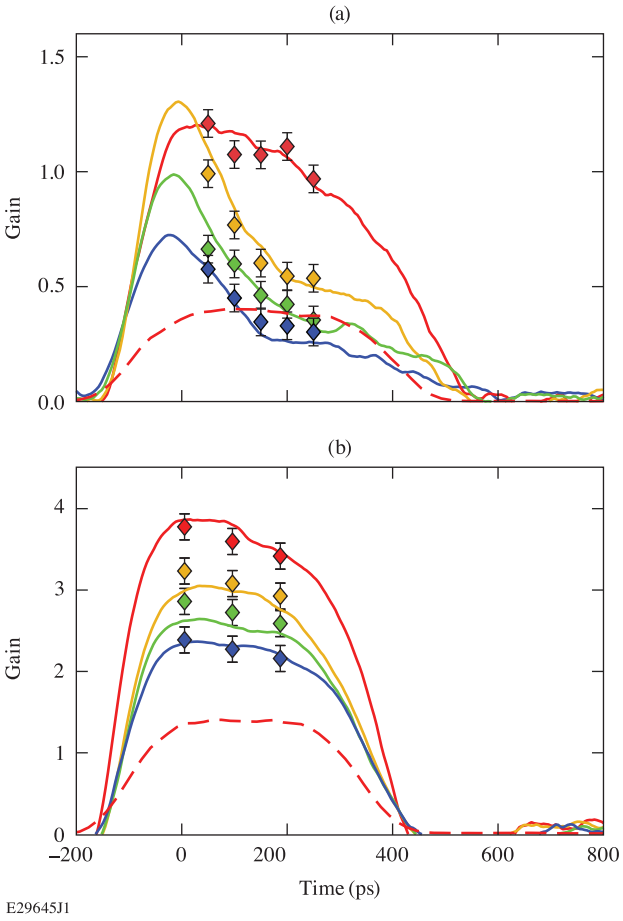

Figure 5. The measured CBET gains $G = \ln(I_1^f/I_1^i)$ (solid curves), pump beam pulse shape (dashed red curve), and kinetic linear theory calculated gains (diamonds) in the (a) high- and (b) low-ion-heating CBET configurations. In the high-ion-heating configuration, the probe beam intensities were 0.1×10^{14} W/cm^2 (red curve), 0.9×10^{14} W/cm^2 (yellow curve), 2.0×10^{14} W/cm^2 (green curve), and 4.1×10^{14} W/cm^2 (blue curve). In the low-ion-heating configuration the probe beam intensities were 0.02×10^{14} W/cm^2 (red curve), 0.4×10^{14} W/cm^2 (yellow curve), 0.8×10^{14} W/cm^2 (green curve), and 1.5×10^{14} W/cm^2 (blue curve).

TOP9 intensity increased which as evident by the drop in the normalized gain. In the low-ion-heating configuration, this saturation was well explained by the depletion of the pump-beam intensity. However, in the high-ion-heating configuration, the impact of pump depletion on gain in the TOP9 beam was negligible.

Figure 6(b) shows the calculated initial ion-heating rates (Eq. 1) that correspond to the TOP9 beam intensities used in the high- and low-ion-heating configurations. When accounting for pump depletion, the high-ion-heating configuration results in significantly more ion heating than the low-ion-heating configurations at equivalent probe beam intensities. This enhanced heating rate was due to the larger CBET scattering energy efficiency ($\eta_{high}/\eta_{low} \sim 2.5$) and shorter interaction length ($L_{high}/L_{low} \sim 0.3$) in

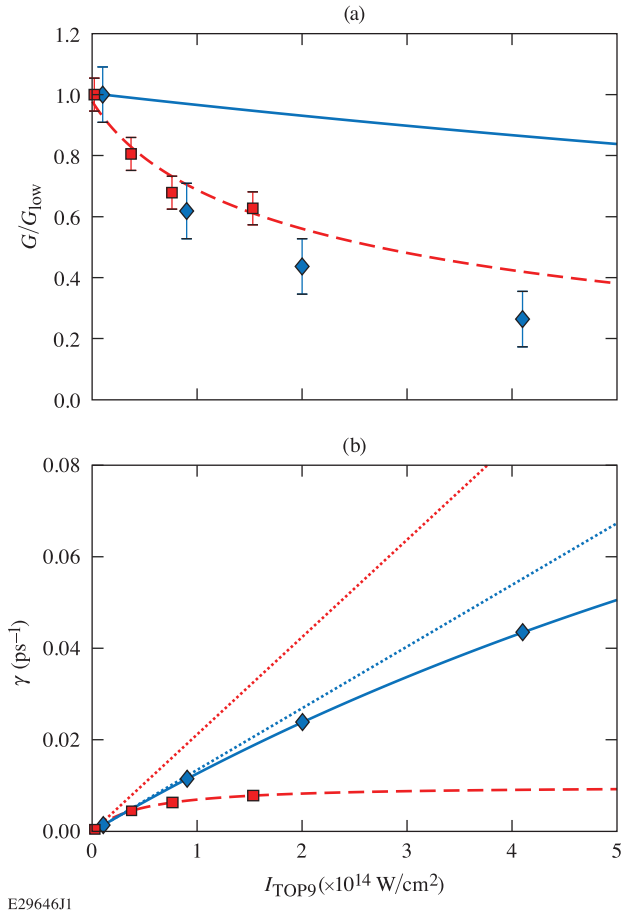

Figure 6. The (a) measured (points) normalized gain at (t=300 ps) and (b) calculated initial (t=0 ps) ion-heating rates for the high- (blue diamonds) and low- (red squares) ion-heating configurations. The solid-blue and dashed-red gain curves represent the (a) expected drop in gain due to pump depletion and the (b) calculated initial ion-heating rates accounting for pump depletion. The (b) dotted curves represent the calculated initial ion-heating rates without pump depletion.

the high-ion-heating configuration. Pump depletion in the low-ion-heating configuration significantly reduces the ion-heating rate at large probe beam intensities ($I_1 > 0.02 \times 10^{14}$ W/cm^2). Here pump depletion rapidly decreases the gain and limits the energy transfer as the probe-beam intensity is increased. In the high-ion heating configuration pump depletion had a negligible effect on the ion heating rate.

3.2. Kinetic Linear CBET Calculations

The linear kinetic CBET theory gain [5] for each TOP9 beam intensity was calculated (Figs. 1 and 5) using the measured plasma conditions, while accounting for pump depletion. Excellent agreement between linear kinetic CBET theory and the measured CBET gains was found when accounting for the ion heating and pump depletion effects.

The gains were calculated as described by Michel *et al.* [27] for the plasma conditions measured with Thomson scattering. The gain in the probe beam was given by $G_0 = gLa_{0s}^2$, where $a_{0s} \approx 8.55 \times 10^{-10}(I_s\lambda_{\mu\rm m}^2)^{1/2}$ is the s-component of the pump beam amplitude, I_{0s} is the s-component of the pump beam intensity in (W/cm^2), and $\lambda_{\mu\rm m}^2$ is the pump beam wavelength in μm. The gain coefficient is given by

$$g = -\frac{k_1 \sin(\theta/2)\tan(\theta/2)}{\sqrt{1-n_e/n_{cr}}}\mathrm{Im}[K], \tag{2}$$

where the coupling factor is given by,

$$K = \frac{\chi_e(1+\chi_i)}{(1+\chi_e+\chi_i)}, \tag{3}$$

and where the electron and ion susceptibilities were numerically calculated for each particles species s using,

$$\chi_s(\mathbf{k},\omega) = \frac{1}{k^2\lambda_{Ds}^2}\int dx \frac{\partial f_s/\partial x}{x_s - x}, \tag{4}$$

where the ion susceptibility is summed over each ion species $\chi_i = \sum_s \chi_s$, λ_{Ds} is the species Debye length, $x_s = \omega/kv_{Ts}$, v_{Ts} is the thermal velocity of species s, and f_s is the 1-D projection of the particle velocity distribution function. In these studies, the ion distribution function was assumed to be Maxwellian ($m = 2$) and the electron distribution was measured to be super-Gaussian ($m \simeq 2.8$) [26], where the measurements were consistent with inverse bremsstrahlung heating [28, 29, 30].

The 1D co-propagating Tang formula [31] was used to account for pump depletion when calculating the gain,

$$e^{G_{Tang}} = \frac{(1+\beta)\exp[G_0(1+\beta)]}{1+\beta\exp[G_0(1+\beta)]}, \tag{5}$$

where $\beta = I_1^i/I_0^i$ is the initial ratio of probe to pump beam intensity and the gain occurs over the average 3D interaction length $L = d/\sin(\theta)$.

The beams were treated as plane waves with area averaged intensity despite the distribution of speckle intensities produced by the phase plates. This approximation is valid due to the large number of both high- and low- intensity speckles that are sampled in the CBET interaction [32].

3.3. Particle-In-Cell Simulations

Figure 7 shows the 1-D ion-velocity distribution functions along the direction of the ion-acoustic wavevector from 2-D VPIC simulations [11, 33] of a high-ion-heating configuration CBET interaction [14]. On short timescales the interaction shows evidence of nonlinear trapping physics but on long timescales the interaction is well described by linear kinetic CBET

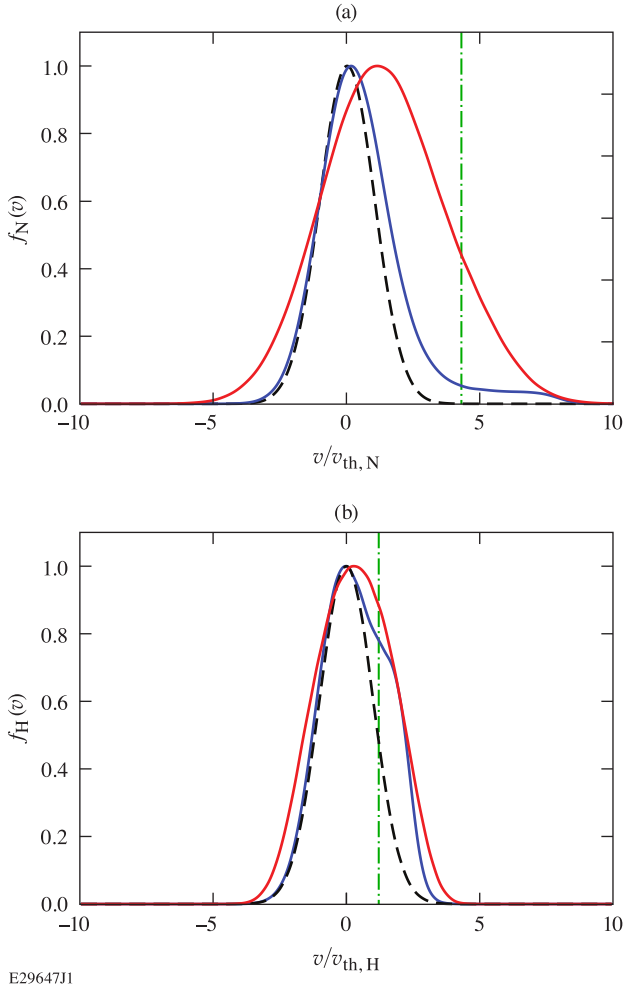

Figure 7. The 1-D (a) nitrogen and (b) hydrogen ion-velocity distribution functions normalized to the initial ion thermal velocities and projected onto the driven ion-acoustic wavevector from a VPIC simulation of the high-ion-heating configuration at a high-probe beam intensity measured at $t = 0$ ps (dashed black curve), $t = 10$ ps (solid blue curve), and $t = 100$ ps (solid red curve). The ion-acoustic wave phase velocity is shown as a vertical line for reference (dotted-dashed green line).

theory. After 10 ps into the interaction, the ion-acoustic waves have grown to large amplitudes and the ion velocity distribution functions show evidence of significant trapping along the ion acoustic wavevector. Here, the phase velocity of the wave is $v_{ph} \sim v_{th,H} \sim 4v_{th,N}$ and consequently there was a large number of hydrogen ions at the wave's phase velocity. At these early times, the number of trapped hydrogen ions was significantly larger than the number of trapped nitrogen ions. However, these hydrogen ions quickly collided and transferred their energy to the nitrogen ions. Later in time (100 ps), the ion-velocity distribution functions showed evidence of isotropic heating. After being initialized with ion temperatures of 150 eV, the ions reached temperatures of $T_{i,N} \sim 450$ eV and $T_{i,H} \sim 250$ eV for the nitrogen and hydrogen ion species, respectively. The larger amount of heating in the nitrogen ions was due to the fact that the trapped hydrogen ions primarily collide with and transfer their kinetic energy to the nitrogen ions. Here, the energy loss collision frequency is a factor of 3.5 larger for H-N collisions than for H-H collisions due to the high nitrogen ionization state ($Z_N = 7$). As the ion heating occurs, the hydrogen thermal velocity quickly exceeds the wave's phase velocity while the nitrogen thermal velocity remains below the wave's phase velocity. The lower nitrogen thermal velocity relative to hydrogen allows the nitrogen ions to continue to Landau damp and absorb energy from the ion-acoustic wave.

These relativistic, electromagnetic particle-in-cell simulations were performed using the code VPIC [11, 33]. Here, a binary collision model was employed to match the Landau form of inter-particle collisions for weakly coupled plasmas [34]. For the simulations presented in this work, ion-ion collisions were included but electron-ion collisions were not. The electron conditions measured in the experiment using Thomson-scattering indicate that the electron-ion energy transfer rates are low and negligible on the time scales relevant to these studies. The simulation domain was reduced relative to the experiment at 138×108 μm with a cell size equal to the Debye length and 512 computational particles per cell per species. The pump and probe beams used random distributions of f/6.7 speckles that had 2.8 μm widths and 99 μm lengths. The boundaries of the simulation box were absorbing for the fields and "refluxing" for the particles. Refluxed particles had velocities randomly sampled from the initial particle velocity distribution functions which were Maxwellian for the ions and super-Gaussian for the electrons.

4. Summary

The CBET models that are used to predict implosion performance in integrated ICF models utilize ad hoc multipliers, which motivated these studies of CBET. Targeted experiments isolated CBET physics from hydrodynamic uncertainties and identified the saturation mechanisms by carefully controlling and measuring the plasma conditions in a gas-jet target that was characterized using Thomson-scattering. In these experiments, a frequency shifted probe beam resonantly interacted with several UV pump beams in two different configurations where the beam and plasma conditions determined the energy transfer saturation mechanism. In a low-ion-heating configuration where the gain was high, the energy transfer was saturated through pump depletion. In a high-ion-heating configuration, the energy transfer was saturated through ion-heating induced detuning

of the IAW resonance. Here, the Thomson-scattering measurements indicated up to a factor of 7 times increase in the plasma ion temperatures when CBET was active. Particle-in-cell simulations showed that on short timescales (< 10 ps) the driven ion waves trapped and accelerated the ions that were subsequently detrapped and thermalized through ion-ion collisions, which resulted in ion heating on long timescales (> 10 ps).

Despite the significant nonlinear physics occurring on short timescales, linear kinetic CBET theory reproduced the measured energy transfer over long timescales in both experimental configurations and at all probe beam intensities when accounting for pump depletion and ion-heating effects. These experiments demonstrate the importance of including the feedback from LPI on plasma conditions in order to fully understand the CBET saturation physics.

This material is based upon work supported by the Department of Energy National Nuclear Security Administration under Award No. DE-NA0003856, the University of Rochester, and the New York State Energy Research and Development Authority. LANL work was performed under the auspices of the U.S. Department of Energy by the Triad National Security, LLC Los Alamos National Laboratory, and was supported by the LANL Directed Research and Development (LDRD) Program and the LANL Office of Experimental Sciences Inertial Confinement Fusion program. VPIC simulations were run on the LANL Institutional Computing Cluster Grizzly. This report was prepared as an account of work sponsored by an agency of the U.S. Government. The views and opinions of authors expressed herein do not necessarily state or reflect those of the U.S. Government or any agency thereof.

[1] Randall C J, Albritton J R, and Thomson J J 1981 *Phys. Fluids* **24** 1474
[2] Igumenshchev I V, Edgell D H, Goncharov V N, Delettrez J A, Maximov A V, Myatt J F, Seka W, Shvydky A, Skupsky S, and Stoeckl C 2010 *Phys. Plasmas* **17** 122708
[3] Michel P *et al.* 2009 *Phys. Rev. Lett.* **102** 025004
[4] Strozzi D J, Bailey D S, Michel P, Divol L, Sepke S M, Kerbel G D, Thomas C A, Ralph J E, Moody J D and Schneider M B 2017 *Phys. Rev. Lett.* **118** 025002
[5] Michel P, Rozmus W, Williams E A, Divol L, Berger R L, Town R P J, Glenzer S H, and Callahan D A 2012 *Phys. Rev. Lett.* **109** 195004
[6] Davis A K *et al.* 2016 *Phys. Plasmas* **23** 056306
[7] Glenzer S H, Divol L M, Berger R L, Geddes C, Kirkwood R K, Moody J D, Williams E A, and Young P E 2001 *Phys. Rev. Lett.* **86** 2565
[8] Kirkwood R K *et al.* 2002 *Phys. Rev. Lett.* **89** 215003
[9] Turnbull D *et al.* 2018 *Plasma Phys. Control. Fusion* **60** 054017
[10] Cohen B I, Lasinski B F, Langdon B A, and Williams E A 1997 *Phys. Plasmas* **4** 956
[11] Yin L, Albright B J, Stark D J, Nystrom W D, Bird R F, and Bowers K J 2019 *Phys. Plasmas* **26** 082708
[12] Chapman T, Brunner S, Banks J W, Berger R L, Cohen B I, and Williams E A 2014 *Phys. of Plasmas* **21** 042107
[13] Chapman T, Berger R L, Cohen B I, Banks J W, and Brunner S 2017 *Phys. Rev. Lett.* **119** 055002
[14] Nguyen K L, Yin L, Albright B J, Hansen A M, Froula D H, Turnbull D, Follett R K, and Palastro J P 2021 *Phys. Plasmas* **28** 082705
[15] Manley J M and Rowe H E 1956 *Proc. IRE* **44** 904
[16] Michel P, Rozmus W, Williams E A, Divol L, Berger R L, Glenzer S H, and Callahan D A 2013 *Phys. Plasmas* **20** 056308
[17] Hansen A *et al.* 2021 *Phys. Rev. Lett.* **126** 075002
[18] Boehly T R *et al.* 1995 *Rev. Sci. Instrum.* **66** 508
[19] Hansen A M, Haberberger D, Katz J, Mastrosimone D, Follett R K, and Froula D H 2018 *Rev. Sci. Instrum.* **89** 10C103
[20] Kruschwitz B E *et al.* 2019 *Proc. SPIE* **10898** 1089804
[21] Boehly T R, Smalyuk V A, Meyerhofer D D, Knauer J P, Bradley D K, Craxton R S, Guardalben M J, Skupsky S, and Kessler T J 1999 *J. Appl. Phys.* **85** 3444
[22] Hubbell J H 1965 *J. Res. Natl. Bur. Stand.* **69C** 139
[23] Katz J, Turnbull D, Kruschwitz B E, Rigatti A L, Rinefierd R, and Froula D H 2021 *Rev. Sci. Instrum.* **92** 033526
[24] Katz J, Boni R, Sorce C, Follett R, Shoup III M J, and Froula D H 2012 *Rev. of Sci. Instrum.* **83** 10E349
[25] Froula D H, Glenzer S H, Luhmann N C, Jr, and Sheffield J 2011 *Plasma Scattering of Electromagnetic Radiation: Theory and Measurement Techniques* 2nd ed. (Amsterdam: Academic Press)
[26] Milder A L, Le H P, Sherlock M, Franke P, Katz J, Ivancic S T, Shaw J L, Palastro J P, Hansen A M, Begishev I A, Rozmus W, and Froula D H 2020 *Phys. Rev. Lett.* **124** 025001
[27] Michel P, Divol L, Turnbull D, and Moody J D 2014 *Phys. Rev. Lett.* **113** 205001
[28] Langdon A B 1980 *Phys. Rev. Lett.* **44** 575
[29] Matte J P, Lamoureux M, Moller C, Yin R Y, Delettrez J, Virmont J, and Johnston T. W. 1988 *Plasma Phys. Control. Fusion* **30** 1665
[30] Turnbull D, Colaïtis A, Hansen A M, Milder A L, Palastro J P, Katz J, Dorrer C, Kruschwitz B E, Strozzi D J, and Froula D H 2020 *Nat. Phys.* **16** 181
[31] Tang C L 1966 *J. Appl. Phys.* **37** 2945
[32] Follett R K, Edgell D H, Froula D H, Goncharov V N, Igumenshchev I V, Shaw J G, and Myatt J F 2017 *Phys. Plasmas* **24** 103128
[33] Yin L, Albright B J, Rose H A, Montgomery D S, Kline J L, Kirkwood R K, Michel P, Bowers K J, and Bergen B 2013 *Phys. Plasmas* **20** 012702
[34] Takizuka T and Abe H 1977 *J. Comput. Phys.* **25** 205
[35] McKinstrie C J, Li J S, Giacone R E, and Vu H X 1996 *Phys. Plasmas* **3** 2686